Boosted Intracavity Aperture in Macrocyclic Amines Enabling Finely Regulated Microporous Membranes

Han, Shuangqiao ; Lu, Zhen ; Zhu, Junyong ; Mai, Zhaohuan ; Matsuyama, Hideto ; He, Tao ; Zhang, Yatao

(Citation)
Nano Letters,24(40):12382-12389

(Issue Date)
2024-09-11

(Resource Type)
journal article

(Version)
Accepted Manuscript

Boosted intracavity aperture in macrocyclic amines enabling finely regulated microporous membranes

Shuangqiao Han,[1†‡] Zhen Lu,[1†] Junyong Zhu,[†] Zhaohuan Mai,[§]* Hideto Matsuyama,[§] Tao He,[#] Yatao Zhang[†]**

[†] School of Chemical Engineering, Zhengzhou University, Zhengzhou 450001, China.

[‡] School of Materials Science and Engineering, North China University of Water Resources and Electric Power, Zhengzhou 450045, China.

[§] Research Center for Membrane and Film Technology, Kobe University, 1-1 Rokkodaicho, Nada, Kobe, 657-8501, Japan

[#] Laboratory for Membrane Materials and Separation Technologies, Shanghai Advanced Research Institute, Chinese Academy of Sciences, Shanghai 201210, China.

[1] These authors contributed equally to this work.

*Corresponding author. Email: zhaohuan.mai@people.kobe-u.ac.jp, zhujunyong@zzu.edu.cn, zhangyatao@zzu.edu.cn

Abstract

Finely tuning the pore structure of traditional nanofiltration (NF) membranes is challenging but highly effective to achieve efficient separations. Herein, we propose a concept of using macrocyclic amine (1,4,7-triazacyclononane: 3A; 1,4,7,10-tetraazacyclododecane: 4A1 and 1,4,8,11-tetraazacyclotetradecane: 4A2) with different intra-annular apertures to finely modulate the pore structure of microporous membranes via interfacial polymerization (IP). The boost in the intracavity size of the building blocks results in heightened steric hindrance of these amine monomers, leading to controlled increase in membrane pore size, as demonstrated by both film characterizations and multiscale simulations. In conjunction with the increased intracavity size, the water permeability follows an augmented trend of 3A-TMC, 4A1-TMC, and 4A2-TMC (TMC: trimesoyl chloride) while exhibiting increased molecular weight cut-offs due to larger free-volume elements and stronger pore interconnectivity. Our proposed macrocyclic amines design strategy provides guideline for finely regulated microporous membranes with high potential in NF-related applications.

Keywords: *Nanofiltration, interfacial polymerization, macrocyclic amine*, *free-volume elements, microporous membranes*

The growing scarcity of water resources and the degradation of aqueous environments present a significant challenge to green and sustainable development.[1-4] The effective usage of brackish water holds great potential for supplying abundant freshwater and mitigating the environmental crisis.[5-8] Nanofiltration (NF) membranes with sub-2-nm micropores and amendable surface charges have demonstrated extensive applications in ion differentiation, removal of heavy metals or micropollutants, water softening, and separation of low-molecular-weight organics.[9-11] In addition, NF membranes exhibit exceptional capabilities in the recovery of critical substances.[12-14]

Polyamide (PA) NF membrane is a type of microporous membrane extensively utilized in molecule/ion separation in liquid systems.[15-17] The PA selective layer is formed via interfacial polymerization (IP) between two reactive monomers, which are present in two immiscible phases respectively.[18-20] Notably, during an IP process, the diffusion of diamine-based molecule from an aqueous solution to organic phase boundary initiates the rapid and irreversible Schotten-Baumann reaction.[21] Such a facile and feasible process frequently renders the formed poly(piperazine amide) membrane high selectivity but low water permeability. This is primarily attributed to the lack of control of the rapid IP process when using piperazine (PIP) and trimesoyl chloride (TMC) as highly reactive monomers, contributing to the formation of highly-crosslinked and thick polyamide films with limited free-volume elements. [22-24]

The usage of macrocyclic monomers could finely adjust the crosslinking degree, as well as increase pore size and porosity of the NF performance.[25, 26] Jiang *et al.* [27] achieved the alignment of functionalized macrocycles (e.g. cyclodextrin, 4-sulfocalix) in polyamide films with ordered channels. Selective amino functionalization of these macrocycles with controlled reactivities allows preferential alignment to form well-defined pore structures within the PA film. In another case, Sun *et al.* [7] reported the

utilization of cucurbit[6]uril molecules (CB, n=6, 8) to endow the PA layer with nanostrand surface structures. The structure of diethylenetriamine (DETA)-CB6 rotaxane was constructed via the host guest interaction, thus resulted in many nanochain patterns on the PA surface. However, the majority of amine monomers exhibit high reactivity, leading to formation of highly-crosslinked PA films and resulting in an inconspicuous enhancement in membrane separation performance.[28-30] In contrast, novel water-phase monomers with larger internal micropores could enable an increase in the pore connectivity of the membrane, thereby facilitating the enhancement of the permeability and selectivity.[31, 32]

Macrocyclic amines are a class of cyclic compounds with secondary amine groups, akin to that of piperazine. The multiple secondary amine groups in these compounds enable them to complete IP reactions with TMC, resulting the formation of structurally stable PA nanofilms.[33-35] Furthermore, compared with PIP, macrocyclic amines offer distinct advantages in the design of PA membranes with improved mono/bivalent salt selectivity. As the number of carbon or nitrogen atoms within the macrocyclic amine increases, their intracavity size also further enlarge.[36-38] Concurrently, the augmented steric hindrance diminishes the reaction efficiency of macrocyclic amines, thereby partially reducing the cross-linking degree of the PA membrane and yielding larger through-nanopores. This ultimately leads to the formation of selective microchannels.[39, 40]

We proposed a concept of using macrocyclic amine with different intra-annular apertures (1,4,7-triazacyclononane: 3A; 1,4,7,10-tetraazacyclododecane: 4A1 and 1,4,8,11-tetraazacyclotetradecane: 4A2) to regulate the pore structure of microporous membranes via IP reaction with TMC (Figure 1a-b). The regulation on the number of nitrogen and carbon atoms in the ring enables controllable increase in the free volume

of the polyazacyclamide membranes. Experimental and simulation results confirmed that a larger inner cavity of macrocyclic amine led to a larger free volume and higher microporosity in amine-TMC PA membranes. Their MWCOs and water fluxes followed the order of 3A-TMC < 4A1-TMC < 4A2-TMC.

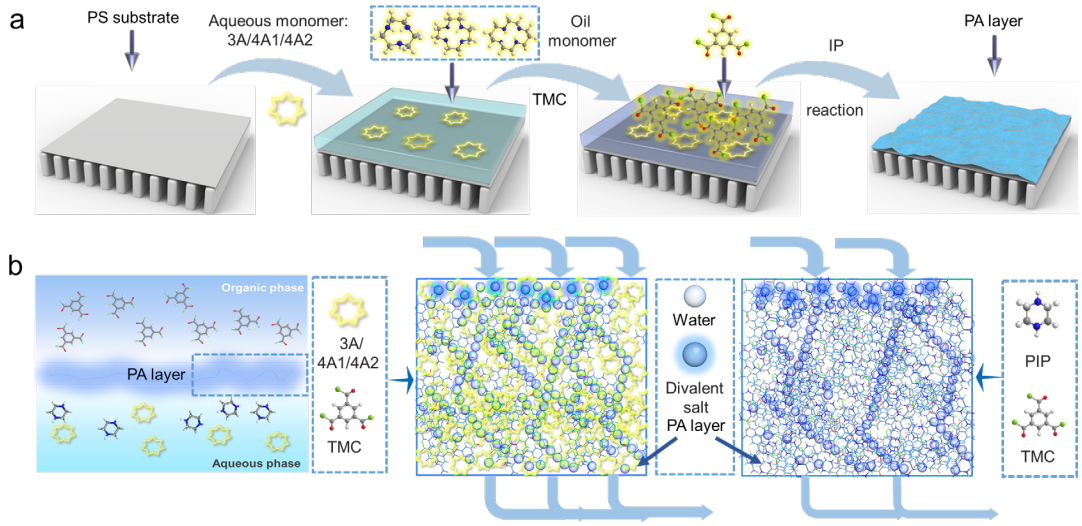

Figure 1. Schematic of polyazacyclamide membranes. (a) Preparation of the polyazacyclamide membrane. (b) The interfacial polymerization process of polyazacyclamide membrane and PIP-TMC polyamide membrane.

Prior to the synthesis of thin-film composed (TFC) membranes, the IP reaction between N-heterocyclic monomers and TMC at free water-hexane interface was conducted to assess the film-forming characteristics (Figure 2a). Visually pliable and continuous films were rapidly formed at the interface within 3 minutes, with no discernible defects on the surface. This observation indicates the high reactivity and film-forming properties at the interface between macrocyclic amines and TMC. Figure S1 depicts the molecular formulas of these nitrogen-containing cyclic monomers, all of which with secondary amines allow rapid polymerization with TMC at the water-hexane interface (Figure S2). In addition, the intracavity sizes of 3A, 4A1 and 4A2

monomers are around 3.3 Å, 3.5 Å and 3.9 Å, respectively (Figure S1), indicating that the intracavity size could be regulated via changing the number of C/N atoms of the macrocyclic amines. Figure S3 displays polyazacyclamide networks of the three amine-TMC systems after crosslinking via MD simulations. As shown in Figure S4a, the results indicate that the broad peak at 1440 and 1360 cm^{-1} assigned to N-H stretching vibrations, and the peak at 1650 cm^{-1} correspond to C=O stretching vibrations, which confirmed the successful formation of the polyazacyclamide.

It can be seen from Figure 2b, the BET surface areas of polyazacyclamide films follow the sequence of freestanding film-1 (3A-TMC: 5.6 $m^2 g^{-1}$) < film-2 (4A1-TMC: 9.4 $m^2 g^{-1}$) < film-3 (4A2-TMC: 39.7 $m^2 g^{-1}$). The calculation based on BET test (Figure 2c) reveals that reveals that all three polyazacyclamide films have abundant microporous structures with pore sizes of 0.22, 0.28 and 0.32 nm for 3A-TMC, 4A1-TMC and 4A2-TMC freestanding films, respectively. As shown in Figure S4b, the calculated average chain *d*-spacing values obtained from the XRD spectrum using Bragg law are 0.34 nm, and 0.33 nm and 0.43 nm, respectively. These findings reveal that the three types of polyazacyclamide films are predominantly comprised of micropores (0.2-0.5 nm), and the increase in the C/N atomic number in the heterocyclic ring leads to an augmentation in the free volume and pore size of as-formed free-standing films. As shown in Figure S5, the diffusion coefficients of 3A, 4A1 and 4A2 monomers are 7.16, 5.35 and 3.83×10^{-10} $m^2 s^{-1}$, respectively. Compared with 3A molecule, 4A2 exhibited lower diffusion rate due to larger intracavity size and steric hindrance, which leads to less available reactive 4A2-TMC pairs in the reaction zone

at the water/*n*-hexane interface, and consequently generating less crosslinked films with larger free volume.

TFC membrane was further prepared on PSf substrate. As shown in Figure 2d, 3A-TMC membranes show a relatively smooth and nodular surface composed of dense spherical particles, and the surface roughness (R_q) of this membrane is 7.53 nm (Figure S6c). Analogously, the 4A1-TMC membrane surface displays a particle-like structure (Figure 2e), with an R_q of 5.61 nm (Figure 2g and S6f). The structure of the 4A2-TMC membrane exhibits significant differences, showing nanobubble-like structures with uniformly diameter and a higher R_q of 8.31 nm (Figure 2f and S6g-i). During the IP process, 4A2 molecules with large steric hindrance may lead to uneven diffusion toward organic interface. This inevitably causes uncontrollable heat release, generating a rougher membrane surface.

As shown in Figures 2i and Figures S7, the average thicknesses of the selective layers for the 3A-TMC, 4A1-TMC and 4A2-TMC membranes are ~50, ~30, and ~25 nm, respectively, which is consistent with the cross-sectional SEM images (Figure S8). To eliminate the influence of the PSf support, the freestanding films were transferred to silicon wafers for analysis of the thickness and morphology characteristics. AFM characterizations also reveal that the thicknesses of the three freestanding films are approximately ~45, ~25, and ~10 nm, respectively (Figure 2h and Figures S9-S11). On the basis of the Freger-Srebnik dynamic theory, the thickness of the polyazacyclamide layer is highly related to the initial film thickness.[41] After the initial film formation, there is a further hinderance to the diffusion of macrocycle amines, which inhibits the growth of the polyazacyclamide membrane. At this stage, the low steric hindrance of the 3A group results in more available reactive groups and a more efficient IP process,

leading to an increase in the thickness of an initial film. The large steric hindrance of 4A2 leads to a lower molecular diffusion rate, hindering the longitudinal growth of polyazacyclamide clusters and consequently forming a thinner selective layer.

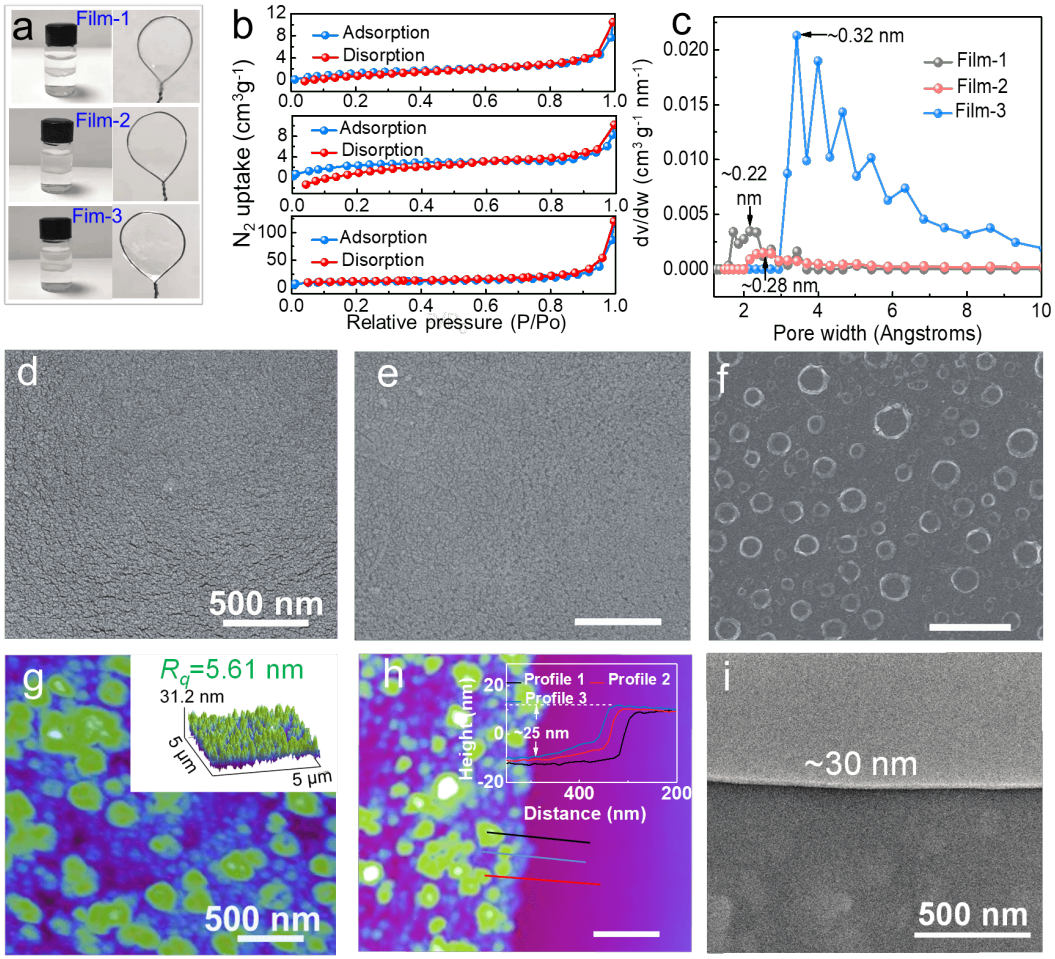

Figure 2. Morphology and thickness of freestanding and TFC polyazacyclamide membranes. (a) Optical image of the freestanding polyazacyclamide membranes. (b) BET curves of freestanding films. (c) pore size distributions for TFC membranes. SEM image: (d) 3A-TMC, (e) 4A1-TMC, (f) 4A2-TMC. 4A1-TMC membrane: (g-h) AFM image, (i) TEM image. Scale bar = 500 nm.

As depicted in Figure S12a, peaks at 1645 cm^{-1} (C=O bond) and 1560 cm^{-1} (C-N bond) elucidate the formation of amide bonds between the macrocyclic amines and TMC in the IP reaction. Based on XPS data, the cross-linking degree of 3A-TMC, 4A1-

TMC, and 4A2-TMC membranes was found to be 59.2%, 50.3%, and 45.6%, respectively (Figure 3a). The 3A-TMC membrane has the highest cross-linking degree, which is in accordance with the lowest surface area of freestanding film-1. This is due to the increase of intracavity size from 3A to 4A2, resulting in an increase in the steric hindrance and a slower diffusion rate of 4A2 molecules, which contributed to the formation of a loose polyazacyclamide network structure. The O1s, N1s, and C1s characteristic peaks of three polyazacyclamide films are presented in Figure 3a, located at 532.1, 400.8, and 284.6 eV, respectively. The peaks in the C 1s spectrum and those in the N 1s spectrum, such as N-H and O-C=N, further confirm the formation of amide bonds (Figure 3b and S12b). Furthermore, the three polyazacyclamide films and the PSf-based membrane exhibit similar thermal stability (Figure S12c).

Figure 3c shows that 3A-TMC membrane exhibits good hydrophilicity due to the less alkyl chain segments and more polar domains. Additionally, the greater hydrophilicity of the 3A-TMC membrane surface is correlated with the decreased surface energy. As shown in Figure 3d, due to the formed -COOH groups on the polyazacyclamide surface, the polyazacyclamide membranes carry a strong negative charge over the wide pH range (over -74 mV). In comparison, the 4A2-TMC membrane is highly negatively charged (-81.2 mV). This is because the surface of the 4A2-TMC membrane possesses less amino groups and more hydrolyzed carboxyl groups, showing negatively charged properties.

The weight cut-offs (MWCOs) of the 3A-TMC, 4A1-TMC and 4A2-TMC membranes are found to be 478, 566, 1499 Da, respectively (Figure 3e). The pore

size distribution (PSD) plot of the composite log-normal model is exhibited in Figure 3f. The average pore size increases from 0.30 nm to 0.46 nm for TFC membranes from 3A-TMC to 4A2-TMC, and the PSD becomes wider. In contrast, the increase in pore size of the 4A2-TMC membrane is largely related to the lower cross-linking degree and the inherent intracavity of the 4A2 molecule.

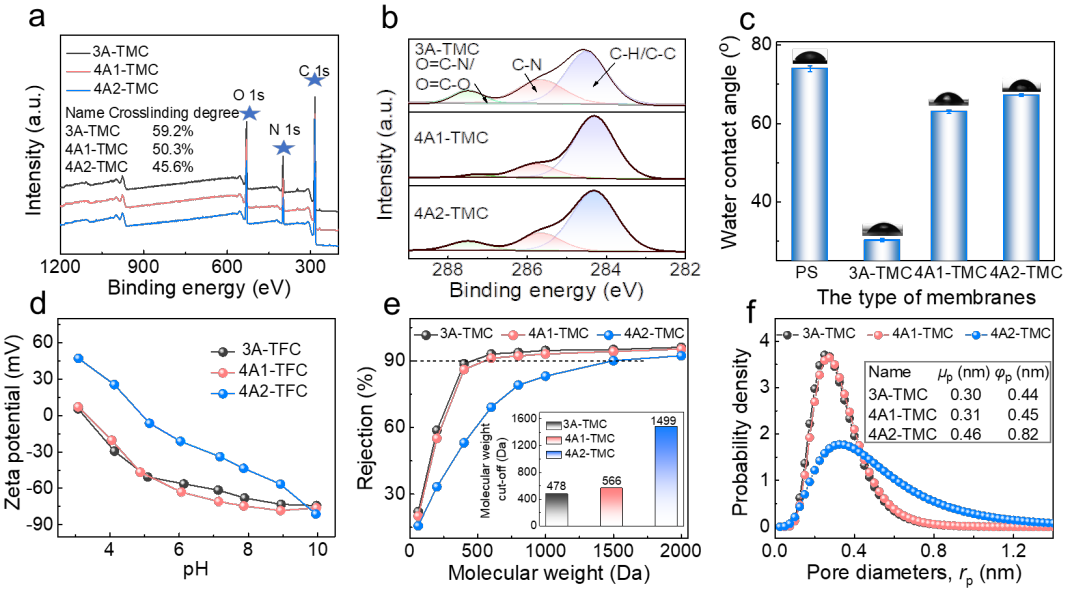

Figure 3. Physicochemical properties of polyazacyclamide membranes. (a) XPS survey spectra. (b) The C1s spectra. (c) Water contact angles. (d) Zeta potentials. (e) MWCOs. (f) PSD.

As depicted in Figure 4a, elevating the aqueous pH enhances the solute rejection followed with a decline of water permeability. This is because the presence of more hydroxide ions efficiently consumes the hydrochloric acid generated from IP reaction and thus facilitates the amide reaction, resulting in an improved crosslinked structure that contributes to enhanced solute rejection. As the 3A concentration changes from 0.1 wt% to 0.2 wt%, the permeability of three polyazacyclamide membranes initially increases rapidly and then drops, primarily relating to changes in the crosslinking degree of the polyazacyclamide films (Figure 4b). As the concentration of the 3A

monomer is 0.18 wt%, a relatively high Na_2SO_4 rejection rate of 97.4% is achieved. Furthermore, it is noted that an increase in macrocyclic amine concentration results in a gradual decrease in water permeability, but the change in rejection rate remains relatively low. This is possibly attributed to the minimal alteration in the crosslinking degree of 3A-TMC membrane as 3A concentration increases (when the concentration of 3A is greater than 0.18 wt%). The optimal IP conditions for the 3A-TMC membrane were obtained with 3A concentration of 0.18 w/v% (pH = 9) and TMC concentration of 0.1 w/v% (Figure S13a), and the TFC membrane was heated at 70°C (Figure S13b) after 1 minute of the IP reaction (Figure 4c). In this context, the attained 3A-TMC membrane exhibits the best performance of 27.3 L m^{-2} h^{-1} bar^{-1} and high rejection (Na_2SO_4: 97.4%). In addition, water molecules (1.38 Å) can pass through two kinds of pore structures (network pore and intracavity) in the polyazacyclamide layer (Figure S14). Therefore, the prepared polyazacyclamide layer provides multicomponent mass transfer channels for the transfer of water molecules.

The same methodology was applied for the regulation of the 4A1-TMC and 4A2-TMC membranes. In contrast, the 4A1-TMC membrane features a thinner polyazacyclamide layer (~25 nm), resulting in an elevated water permeability (34.6 L m^{-2} h^{-1} bar^{-1}) and a Na_2SO_4 rejection of 94.2% (Figures 4d-f and Figures S13c-d). However, as displayed in Figure S15, an increase in the number of C atoms on the macrocyclic amine ring deteriorates the separation performance of the 4A2-TMC membrane. This is largely due to larger steric hindrance of 4A2, leading to the formation of a looser polyazacyclamide film with a wider PSD.

The rejection rates of these polyazacyclamide membranes followed: Na_2SO_4 > $MgSO_4$ > $CaCl_2$~ $MgCl_2$> NaCl (Figure 4g). According to the synergistic Donnan and size sieving effects, the separation mechanism of polyazacyclamide membranes can be summarized as follows. Monovalent hydrated ions have smaller radii (Cl^- < SO_4^{2-}, Na^+ < Ca^{2+} < Mg^{2+}). In this context, polyazacyclamide membranes with abundant negative charges exhibit higher rejection rates for Na_2SO_4 and $MgSO_4$. On the other hand, the electrostatic attraction between divalent cations and the negatively charged active layer promotes the transmission of Mg^{2+} and Ca^{2+}. Due to electrostatic repulsion, the 3A-TMC membrane displays a higher rejection towards the negatively charged divalent SO_4^{2-}, while showing lower rejection towards monovalent NaCl with smaller hydrated ion size. The inorganic salt rejection of 4A1-TMC membrane slightly declines due to the hindered diffusion of 4A1 monomer and the increased interfacial voids. Compared to the 3A-TMC and 4A1-TMC membranes, the 4A2-TMC membrane exhibits lower rejection for inorganic salts. In addition, a mixed salt solution containing 2000 ppm Na_2SO_4 and 4000 ppm NaCl was used to evaluate the separation capacity of Cl^-/SO_4^{2-}. The results showed that the rejection of SO_4^{2-} is more than 90% and the rejection of Cl^- is less than 35% of 3A-TMC and 4A1-TMC membranes, showing good Cl^-/SO_4^{2-} separation coefficient (Figure S16).

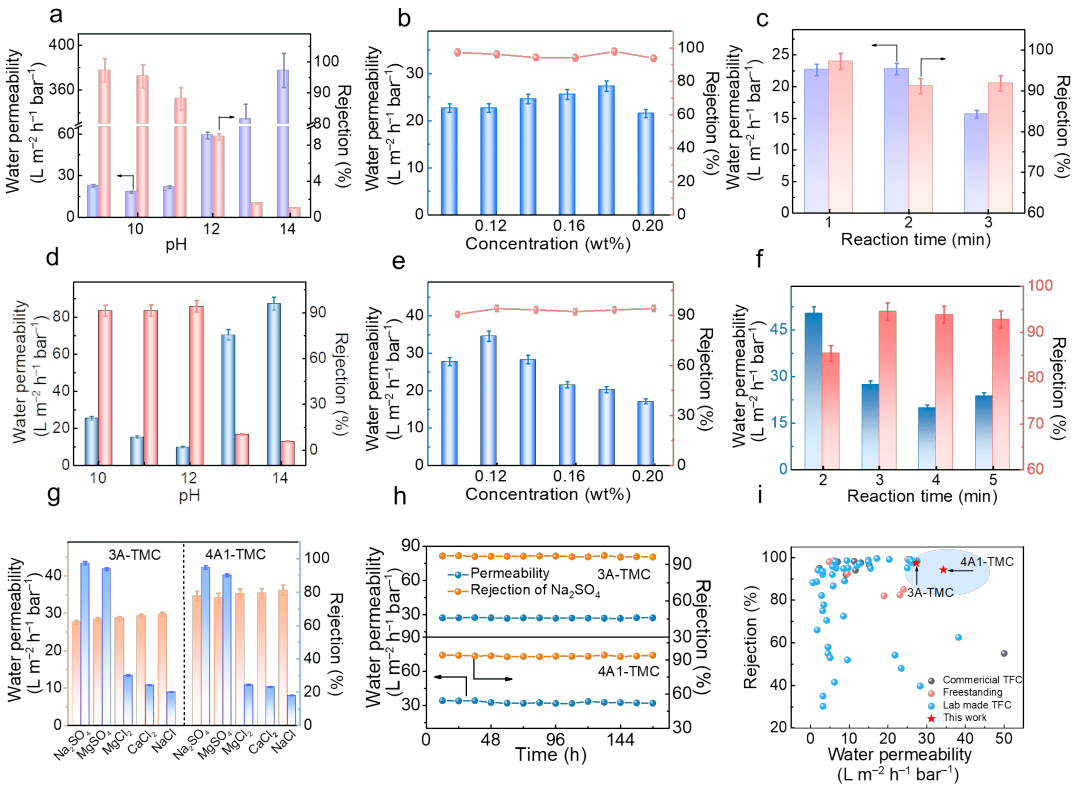

Figure 4. NF performance of polyazacyclamide membranes. Effects of aqueous solution pH on membrane performance (water permeability and Na_2SO_4 rejection): (a) 3A-TMC, (d) 4A1-TMC. Effects of macrocyclic amine concentrations on membrane performance: (b) 3A-TMC membrane, (e) 4A1-TMC membrane. Effects of reaction time on membrane performance: (c) 3A-TMC, (f) 4A1-TMC. (g) NF performance of polyazacyclamide (3A-TMC and 4A1-TMC) membranes for different inorganic salts. (h) Long-term stability of polyazacyclamide membranes. (i) Comparison on NF performance of 3A-TMC and 4A1-TMC membranes with reported NF membranes.[42]

The long-term test of the polyazacyclamide (3A-TMC and 4A1-TMC) membranes is illustrated in Figure 4h. The results indicate that the fabricated polyazacyclamide membranes exhibit high operational stability in continuous crossflow tests over 7 days, with minimal fluctuations in membrane permeance (~26 L m^{-2} h^{-1} bar^{-1}) and salt rejection (> 97%). Furthermore, as shown in Figure 4i, the 3A-TMC and 4A1-TMC

membranes exhibit higher permeance and good Na_2SO_4 rejection, surpassing most commercial TFC membranes, freestanding membranes, and lab made TFC membranes.

Dissipative particle dynamics (DPD) simulations were employed to model the dynamic formation process of the polyazacyclamide layer processes for the prepared membranes (Figure 5 and Figures S17-20). Different functional groups were represented by DPD beads (Figure S17). Before the IP reaction, the macrocyclic amine monomers were uniformly dispersed in the aqueous solution (Figure S18). After the reaction, the macrocyclic amine monomers gradually migrate to the water/oil interface, reaching equilibrium at 400,000 steps (Figure 5a-c).

The density distributions of different beads represent the amine monomers and TMC molecules were shown in Figure 5d-f. Furthermore, we assumed that the density of D beads (-NH- groups in the macrocyclic amine monomer) could be roughly used to estimate the polymeric sites and the low-density sites represent the distribution of the porous sites of the three macrocyclic amine-TMC layers. Figure S19d shows the density distribution of D beads at the interface of the three IP systems. It was indicated that as the number of N and C atoms in the macrocyclic amine monomer increases, more low-density -NH- regions are observed. This suggests that in the macrocyclic amine-TMC system, the 4A2-TMC membrane has a higher porosity, highly consistent with the experimental data.

Figures S19 depict the concentration distribution of different beads along the *y*-axis perpendicular to the interface in each system. The results show that the relative concentration of amino acid is higher in the 3A-TMC membrane system, compared to

the 4A1-TMC and 4A2-TMC membrane systems. This confirms that the 3A monomer has a higher degree of polymerization with TMC, while the steric hindrance effect of the 4A2 monomer significantly restricts the diffusion of the monomer, resulting in a lower monomer concentration in the portrait film growth. Therefore, the macrocyclic amine layer formed in 4A2-TMC membrane system is thinner, leading to a higher water permeability.

A comparison of the 3A monomer system with the PIP-TMC system reveals similar concentrations of amine monomers at the interface, indicating similar cross-linking degrees between the macrocyclic amine monomer and PIP (Figure S20). However, the polyazacyclamide membrane formed based on the 3A monomer has a significantly large pore size. Besides, we tested the performance of PIP-TMC membrane under the same preparation conditions. The fabricated membrane shows a similar inorganic salt rejection to 3A-TFC membrane, but the permeability is only ~10 $L\ m^{-2}\ h^{-1}\ bar^{-1}$ (Figure S21).

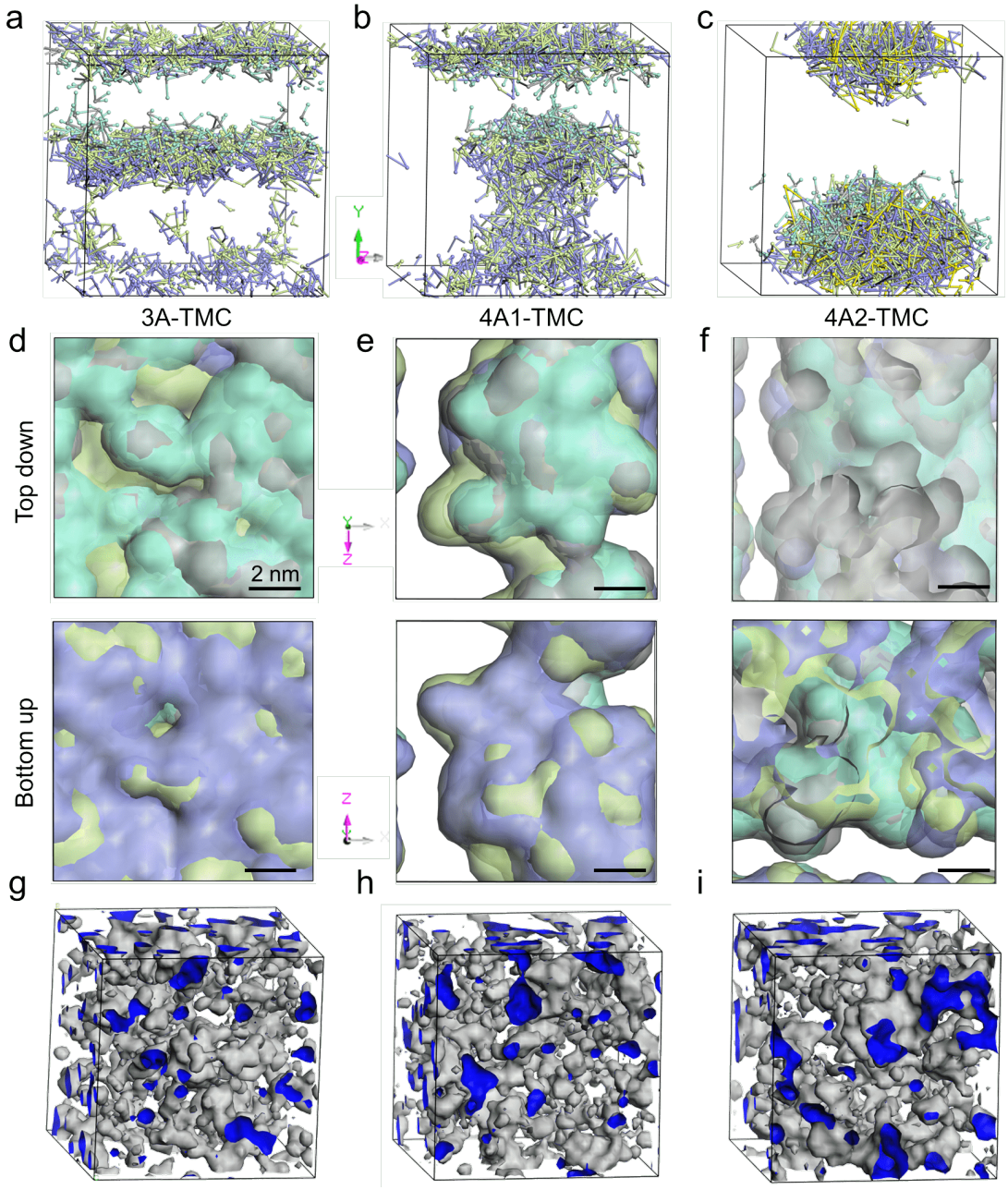

Figure 5. DPD and MD simulations of the IP process. (a-c) Snapshots of the macrocyclic amine /TMC system (t =400,000): (a) 3A-TMC system, (b) 4A1-TMC system, (c) 4A2-TMC system. (d-f) Density distribution of different beads in the three IP systems after IP reactions: (d) 3A-TMC system, (e) 4A1-TMC system, (f) 4A2-TMC system. Top: top-down view of the polyazacyclamide network, Bottom: bottom up view of the polyazacyclamide network. FFV image of macrocyclic amine /TMC system: (g) 3A-TMC system, (h) 4A1-TMC system, (i) 4A2-TMC system.

Molecular dynamics (MD) simulations were used to calculated fraction of free volume (FFV) of the prepared members. It can be seen in Figure 5g-i, from 3A to 4A2 monomer, the FFV containing both interchain and intrachain cavities increased gradually. The macrocyclic amine molecules became slightly disordered after crosslinking, mainly due to their relatively small structures. The corresponding free volumes of the three systems are calculated and the FFV of the three PA membranes followed the order of 3A-TMC (16.58%) ~ 4A1-TMC (16.32%) < 4A2-TMC (17.05%), in fairly good agreement with the experimental data on the MWCOs. In addition, as seen from Figure S22, the low-density area of the polyazacyclamide film (in blue) increased gradually from 3A-TMC to 4A2-TMC membrane, indicating that the pore connectivity of the system from 3A-TMC to 4A1-TMC to 4A2-TMC is gradually enhanced.

In this study, polyazacyclic-amide nanofilms with finely-tuned pore apertures were created through IP process between macrocyclic amines and TMC. The thickness and pore size of the polyazacyclamide selective layer enable adjusted via kinds of macrocyclic amines and the IP conditions. As the number of N and C atoms on the N-heterocycle increases, the monomers show a boosted steric hindrance and declined reactivity, leading to a decrease in crosslinking degrees and thus forming a loosely structured polyazacyclamide layer. By adjusting the IP conditions, the optimized 4A1-TMC membrane has a high water performance of 34.6 L m^{-2} h^{-1} bar^{-1} with a MWCO of 566 Da. The membrane exhibits excellent chemical and mechanical stability, making it potentially feasible in NF-related applications.

Supporting Information

Experimental, characterization methods, membrane performance test, calculation of crosslinking degree, calculation of MWCO and PSD, simulation, supporting figures and tables have been shown as Supporting Information.

Acknowledgment

This work was supported by the National Natural Science Foundation of China (No. 22108257 and 22178327), the Excellent Youth Foundation of Henan Scientific Committee (No. 222300420018), Key Scientific Research Projects in Universities of Henan Province (No. 21zx006), and China Postdoctoral Science Foundation (No. 2022M712872). The simulations and characterizations were tested from the National Supercomputing Center in Zhengzhou and the Center of Advanced Analysis and Computational Science at Zhengzhou University, respectively.

References

1. Wang, Z.; Liang, S.; Kang, Y.; Zhao, W.; Xia, Y.; Yang, J.; Wang, H.; Zhang, X. Manipulating interfacial polymerization for polymeric nanofilms of composite separation membranes. *Prog. Polym. Sci.*, **2021**, *122*, 101450.

2. Di Vincenzo, M.; Tiraferri, A.; Musteata, V. E.; Chisca, S.; Sougrat, R.; Huang, L. B.; Nunes, S. P.; Barboiu, M. Biomimetic artificial water channel membranes for enhanced desalination. *Nat. nanotechnol*., **2021,** *16* (2), 190–196.

3. Yuan, B.; Zhao, S.; Hu, P.; Cui, J.; Niu, Q. J. Asymmetric polyamide nanofilms with highly ordered nanovoids for water purification. *Nat. Commun.*, **2020**, *11* (1), 6102.

4. Porter, C. J.; Werber, J. R.; Zhong, M.; Wilson, C. J.; Elimelech, M. Pathways and Challenges for Biomimetic Desalination Membranes with Sub-Nanometer Channels. *ACS Nano*, **2020**, *14* (9), 10894–10916.

5. Liang, Y.; Zhu, Y.; Liu, C.; Lee, K. R.; Hung, W. S.; Wang, Z.; Li, Y.; Elimelech, M.; Jin, J.; Lin, S. Polyamide nanofiltration membrane with highly uniform sub-nanometre pores for sub-1 A precision separation. *Nat. Commun.*, **2020**, *11* (1), 2015.

6. Huang, T.; Moosa, B. A.; Hoang, P.; Liu, J.; Chisca, S.; Zhang, G.; AlYami, M.; Khashab, N. M.; Nunes, S. P. Molecularly-porous ultrathin membranes for highly selective organic solvent nanofiltration. *Nat. Commun*., **2020**, *11* (1), 5882.

7. Tang, M. J.; Liu, M. L.; Wang, D. A.; Shao, D. D.; Wang, H. J.; Cui, Z.; Cao, X. L.; Sun, S. P. Precisely Patterned Nanostrand Surface of Cucurbituril[n]-Based Nanofiltration Membranes for Effective Alcohol-Water Condensation. *Nano Lett.*, **2020**, 20 (4), 2717–2723.

8. Lu, C.; Hu, C.; Ritt, C. L.; Hua, X.; Sun, J.; Xia, H.; Liu, Y.; Li, D. W.; Ma, B.; Elimelech, M.; Qu, J. In Situ Characterization of Dehydration during Ion Transport in Polymeric Nanochannels. *J. Am. Chem. Soc.*, **2021**, *143* (35),14242–14252.

9. You, X.; Xiao, K.; Wu, H.; Li, Y.; Li, R.; Yuan, J.; Zhang, R.; Zhang, Z.; Liang, X.; Shen, J.; Jiang, Z. Electrostatic-modulated interfacial polymerization toward ultra-permselective nanofiltration membranes. *iScience*, **2021**, *24* (4), 102369.

10. Yang, Z.; Sun, P. F.; Li, X.; Gan, B.; Wang, L.; Song, X.; Park, H. D.; Tang, C. Y. A Critical Review on Thin-Film Nanocomposite Membranes with Interlayered Structure: Mechanisms, Recent Developments, and Environmental Applications.

Environ. Sci. Technol., **2020**, *54* (24), 15563–15583.

11. Song, X.; Gan, B.; Qi, S.; Guo, H.; Tang, C. Y.; Zhou, Y.; Gao, C. Intrinsic Nanoscale Structure of Thin Film Composite Polyamide Membranes: Connectivity, Defects, and Structure-Property Correlation. *Environ. Sci. Technol.*, **2020**, *54* (6), 3559–3569.

12. Lu, X.; Elimelech, M. Fabrication of desalination membranes by interfacial polymerization: history, current efforts, and future directions. *Chem. Soc. Rev.*, **2021**, *50* (11), 6290–6307.

13. Zhang, F.; Fan, J. B.; Wang, S. Interfacial Polymerization: From Chemistry to Functional Materials. *Angew. Chem.*, **2020**, *59* (49), 21840–21856.

14. Sarkar, P.; Modak, S.; Karan, S. Ultraselective and Highly Permeable Polyamide Nanofilms for Ionic and Molecular Nanofiltration. *Adv. Funct. Mater.*, **2020**, *31* (3), 2007054.

15. Peng, H.; Zhao, Q. A Nano-Heterogeneous Membrane for Efficient Separation of Lithium from High Magnesium/Lithium Ratio Brine. *Adv. Funct. Mater.*, **2021**, *31* (14), 2009430.

16. Peng, H.; Zhang, W. H.; Hung, W. S.; Wang, N.; Sun, J.; Lee, K. R.; An, Q. F.; Liu, C. M.; Zhao, Q. Phosphonium Modification Leads to Ultrapermeable Antibacterial Polyamide Composite Membranes with Unreduced Thickness. *Adv. Mater.*, **2020**, *32* (22), e2001383.

17. Gao, S.; Zhu, Y.; Gong, Y.; Wang, Z.; Fang, W.; Jin, J. Ultrathin Polyamide Nanofiltration Membrane Fabricated on Brush-Painted Single-Walled Carbon

Nanotube Network Support for Ion Sieving. *ACS Nano*, **2019**, *13* (5), 5278–5290.

18. Ali, Z.; Ghanem, B. S.; Wang, Y.; Pacheco, F.; Ogieglo, W.; Vovusha, H.; Genduso, G.; Schwingenschlogl, U.; Han, Y.; Pinnau, I. Finely Tuned Submicroporous Thin-Film Molecular Sieve Membranes for Highly Efficient Fluid Separations. *Adv. Mater.*, **2020**, *32* (22), e2001132.

19. Zhang, X.; Liu, C.; Yang, J.; Zhu, C.-Y.; Zhang, L.; Xu, Z.-K. Nanofiltration membranes with hydrophobic microfiltration substrates for robust structure stability and high water permeation flux. *J. Membr. Sci.*, **2020**, *593*, 117444.

20. Guo, M.; Wang, S.; Gu, K.; Song, X.; Zhou, Y.; Gao, C. Gradient cross-linked structure: Towards superior PVA nanofiltration membrane performance. *J. Membr. Sci.*, **2019**, *569*, 83–90.

21. Sheng, F.; Wu, B.; Li, X.; Xu, T.; Shehzad, M. A.; Wang, X.; Ge, L.; Wang, H.; Xu, T. Efficient Ion Sieving in Covalent Organic Framework Membranes with Sub-2-Nanometer Channels. *Adv. Mater.*, **2021**, *33* (44), e2104404.

22. Tan, Z.; Chen, S.; Peng, X.; Zhang, L.; Gao, C. Polyamide membranes with nanoscale Turing structures for water purification. *Science*, **2018**, *360* (6388), 518–521.

23. Teng, X.; Fang, W.; Liang, Y.; Lin, S.; Lin, H.; Liu, S.; Wang, Z.; Zhu, Y.; Jin, J. High-performance polyamide nanofiltration membrane with arch-bridge structure on a highly hydrated cellulose nanofiber support. *Sci. China Mater.*, **2020**, *63*, 2570–2581.

24. Epsztein, R.; DuChanois, R. M.; Ritt, C. L.; Noy, A.; Elimelech, M. Towards single-species selectivity of membranes with subnanometre pores. *Nat. Nanotechnol.*, **2020**, *15* (6), 426–436.

25. Wang, Z.; Wang, Z.; Lin, S.; Jin, H.; Gao, S.; Zhu, Y.; Jin, J. Nanoparticle-templated nanofiltration membranes for ultrahigh performance desalination. *Nat. Commun.*, **2018**, *9* (1), 2004.

26. Liu, J.; Hua, D.; Zhang, Y.; Japip, S.; Chung, T. S. Precise Molecular Sieving Architectures with Janus Pathways for Both Polar and Nonpolar Molecules. *Adv. Mater.*, **2018**, *30* (11), 1705933.

27. Jiang, Z.; Dong, R.; Evans, A. M.; Biere, N.; Ebrahim, M. A.; Li, S.; Livingston, A. G. Aligned macrocycle pores in ultrathin films for accurate molecular sieving. *Nature*, **2022**, *609* (7925), 58–64.

28. Tiwari, K.; Sarkar, P.; Modak, S.; Singh, H.; Pramanik, S. K.; Karan, S.; Das, A.Large Area Self-Assembled Ultrathin Polyimine Nanofilms Formed at the Liquid-Liquid Interface Used for Molecular Separation. *Adv. Mater.*, **2020**, *32* (8), e1905621.

29. Huang, T.; Puspasari, T.; Nunes, S. P.; Peinemann, K. V. Ultrathin 2D-Layered Cyclodextrin Membranes for High-Performance Organic Solvent Nanofiltration. *Adv. Funct. Mater.*, **2019**, *30* (4), 1906797.

30. Zheng, S. P.; Huang, L. B.; Sun, Z.; Barboiu, M. Self-Assembled Artificial Ion-Channels toward Natural Selection of Functions. *Angew. Chem.*, **2021**, *60* (2)**,** 566–597.

31. Karan, S.; Jiang, Z.; Livingston, A. G. Sub-10 nm polyamide nanofilms with ultrafast solvent transport for molecular separation. *Science*, **2015**, *348* (6241), 1347–1351.

32. Wang, J.; Qin, L.; Lin, J.; Zhu, J.; Zhang, Y.; Liu, J.; Van der Bruggen, B. Enzymatic construction of antibacterial ultrathin membranes for dyes removal. *Chem. Eng. J.*,

2017, *323*, 56–63.

33. Gui, L.; Dong, J.; Fang, W.; Zhang, S.; Zhou, K.; Zhu, Y.; Zhang, Y.; Jin, J. Ultrafast Ion Sieving from Honeycomb-like Polyamide Membranes Formed Using Porous Protein Assemblies. *Nano Lett.*, **2020**, *20* (8), 5821–5829.

34. Jiang, C.; Tian, L.; Zhai, Z.; Shen, Y.; Dong, W.; He, M.; Hou, Y.; Niu, Q. J. Thin-film composite membranes with aqueous template-induced surface nanostructures for enhanced nanofiltration. *J. Membr. Sci*, **2019**, *589*, 117244.

35. Zhao, Y.; Zhang, Z.; Dai, L.; Zhang, S. Preparation of a highly permeable nanofiltration membrane using a novel acyl chloride monomer with -$PO(Cl)_2$ group. *Desalination*, **2018**, *431*, 56–65.

36. Zhang, C.; Wei, K.; Zhang, W.; Bai, Y.; Sun, Y.; Gu, J. Graphene Oxide Quantum Dots Incorporated into a Thin Film Nanocomposite Membrane with High Flux and Antifouling Properties for Low-Pressure Nanofiltration. *ACS Appl. Mater. Interfaces*, **2017**, *9* (12), 11082–11094.

37. Boo, C.; Wang, Y.; Zucker, I.; Choo, Y.; Osuji, C. O.; Elimelech, M. High Performance Nanofiltration Membrane for Effective Removal of Perfluoroalkyl Substances at High Water Recovery. *Environ. Sci. Technol.*, **2018**, *52* (13), 7279–7288.

38. Li, N.; Chen, F.; Shen, J.; Zhang, H.; Wang, T.; Ye, R.; Li, T.; Loh, T. P.; Yang, Y. Y.; Zeng, H. Buckyball-Based Spherical Display of Crown Ethers for De Novo Custom Design of Ion Transport Selectivity. *J. Am. Chem. Soc.*, **2020**, *142* (50), 21082–21090.

39. Liang, B.; Wang, H.; Shi, X.; Shen, B.; He, X.; Ghazi, Z. A.; Khan, N. A.; Sin, H.; Khattak, A. M.; Li, L.; Tang, Z. Microporous membranes comprising conjugated

polymers with rigid backbones enable ultrafast organic-solvent nanofiltration. *Nat. Chem.*, **2018**, *10* (9), 961–967.

40. Li, B.; Japip, S.; Chung, T. S. Molecularly tunable thin-film nanocomposite membranes with enhanced molecular sieving for organic solvent forward osmosis. *Nat. Commun.*, **2020**, *11* (1), 1198.

41. V, Freger. Nanoscale heterogeneity of polyamide membranes formed by interfacial polymerization. *Langmuir*, **2003**, ***19*** (11), 4791–4797.

42. Yang, Z.; Long, L.; Wu, C.; Tang, C. Y. High permeance or high selectivity? Optimization of system-scale nanofiltration performance constrained by the upper bound. *ACS. EST. Eng.*, **2022**, *2* (3), 377–390.

TOC graphic:

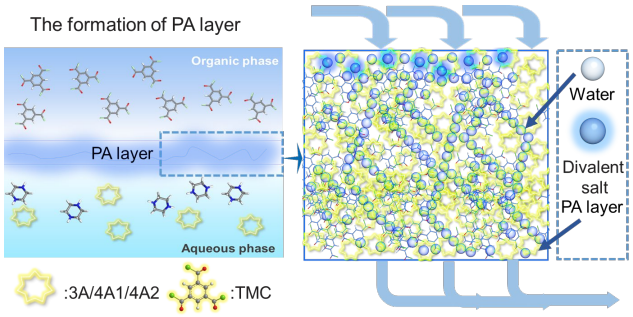
The formation of PA layer
Organic phase
PA layer
Aqueous phase
:3A/4A1/4A2
:TMC
Water
Divalent salt
PA layer